ACS Catalysis

pubs.acs.org/acscatalysis Research Article

Kinetics of Acid-Catalyzed Dehydration of Alcohols in Mixed Solvent Modeled by Multiscale DFT/MD

Bolton Tran, Scott T. Milner, and Michael J. Janik*

Cite This: ACS Catal. 2022, 12, 13193−13206 Read Online

ACCESS | Metrics & More | Article Recommendations | Supporting Information

ABSTRACT: Acid-catalyzed alcohol dehydration is a key reaction step in biomass upgrading, kinetics of which are significantly affected by mixed aqueous solvents. Computational modeling can provide fundamental understanding of solvation effects in catalysis, and ultimately a predictive tool for optimizing reactivity and selectivity. We introduce a multiscale method that combines density functional theory (DFT) with classical molecular dynamics (MD) to investigate the effect of mixed solvents (water with DMSO/GVL/MeCN) on the kinetics of acid-catalyzed dehydration of *t*-butanol and fructose. We determine the thermodynamically stable form of the excess proton (*i.e.*, the catalyst) in mixed solvents. In water/GVL and water/MeCN mixtures, the excess proton resides on a water cluster ($H_5O_2^+$). In water/DMSO, it forms a DMSO-H_3O^+ cluster in a bulk water/DMSO mixture, but appears as $H_5O_2^+$ when close to an alcohol reactant. We model the E1 dehydration mechanism on *t*-butanol and fructose with DFT, and subsequently solvate each reaction intermediate and transition state with MD. Reaction free energy profiles for the elementary steps are mapped out at different solvent compositions. Our predictions compare well to results of Mellmer *et al.* Nature Catalysis **2018**, 1, 199−207 and Nature Communications **2019**, 10, 1−10, for both AIMD-measured reaction free energy profiles and experimental rate constants. By decoupling the gas-phase and solvation free energies, our calculation provides a clear interpretation of the solvation effects on an absolute free energy scale, and furthermore deconvolutes these effects into intuitive short-range electronic and longer range electrostatic interactions. Furthermore, our approach reveals solvent structuring around the reaction intermediates and the transition state. Our scalable DFT/MD approach provides a potentially powerful tool to predict reaction kinetics in condensed phases as well as detailed structural and energetic understanding of solvation effects in catalysis.

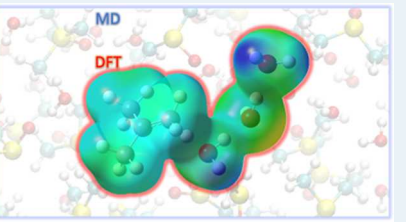

KEYWORDS: *acid catalysis, homogeneous catalysis, solvation effect, mixed solvent, QM/MM, multiscale modeling*

INTRODUCTION

Upgrading lignocellulosic biomass into valuable chemicals and fuels requires selectively transforming bulky organic molecules into desired products.[1] Biomass upgrading reactions are often catalyzed by Brønsted acid in aqueous solution. For example, alcohol dehydration is an acid-catalyzed reaction that removes a hydroxyl (−OH) group to form an unsaturated C═C bond.

To improve the activity and selectivity of acid-catalyzed biomass reactions, different proton carriers and solvents can be considered. Heterogeneous catalysts such as metal−organic frameworks[2] and zeolites[3,4] are robust candidates for the proton carrier. These catalysts both provide adsorption sites for stabilizing the reaction intermediates and transition states and act as Brønsted acid with a tunable proton dissociation free energy. Alternatively, solvent molecules can act as the proton carrier in homogeneous catalysis system. Water is a common solvent for biomass conversion; addition of aprotic co-solvents significantly alters the kinetics of acid-catalyzed biomass reactions[5,6] by differentially solvating reactive intermediates and transition states.[7] Tuning the interactions between the reactive species, the catalyst and the (mixed) solvent provides a powerful design space for optimizing kinetics of biomass reactions.

Computational modeling can help rationally design the optimal sets of catalysts and solvents for biomass reactions, and solution-phase acid-catalyzed reactions in general.[8] In this paper, we present a multiscale computational approach that combines density functional theory (DFT) with classical molecular dynamics (MD) to model the kinetics of acid-catalyzed reactions in the solution phase. Below, we first review different computational methods to model solution-phase chemistry, motivating our DFT/MD approach. We then introduce our specific study: modeling the effect of aprotic co-solvents on the kinetics of homogeneous acid-catalyzed alcohol dehydration reactions.

Computational Model for the Solution-Phase Reaction. An atomistic computational approach to model the thermodynamics and kinetics of a solution-phase reaction must accomplish two goals. First, it must describe how the energy

Received: August 11, 2022
Revised: September 30, 2022
Published: October 14, 2022

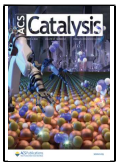

changes when chemical bonds form or break. This requires a quantum mechanical treatment. Second, it must describe how the solvent stabilizes different extrema along the reaction coordinate. This requires sampling of the fluctuating solvent configurations around the reactive center, which alter the free energies of the reaction intermediates and transition states. For homogeneous acid-catalyzed reactions, the solvent can take part in the reaction coordinate, acting as either the donor or acceptor of a proton (*e.g.*, water as H_3O^+ or $H_5O_2^+$ complexes).

Ab initio MD (AIMD) has been used to study the reaction kinetics of solution-phase reactions.[6,9,10] AIMD treats both the reaction and solvent coordinates at the quantum mechanical (*e.g.*, DFT) level of theory. However, AIMD is computationally expensive: AIMD simulations with state-of-the-art algorithms and processors can only tractably model roughly several hundreds of atoms for tens of picoseconds. With such a short timescale, reactions with high activation barriers must be accelerated with non-equilibrium enhanced sampling techniques.[11] These enhanced sampling techniques require representing the reaction coordinates in terms of some collective variables defined from various atomic distances. For simpler homogeneous acid-catalyzed reactions such as hydride shift or dehydration, the mechanism is known and the collective variables are straightforward to define and use.[9,10,12] Even with enhanced sampling, AIMD sampling of solvent coordinates, especially for mixed solvents around a charged solute, is still limited by its short time and length scale. Furthermore, given the vast number of reactions in a biomass upgrading network, coupled with numerous possible co-solvents, proton carriers, and counterions to choose from, it is challenging to use only AIMD to explore this design space. This motivates the development of "faster" computational tools, as well as simple design rules for modeling the kinetics of acid-catalyzed reactions in mixed solvents.[7]

Ab initio methods can be combined with implicit solvation models to avoid the solvent sampling limitation by instead treating the solvent as a continuum. However, these models sacrifice atomistic description and are unreliable if not specifically parameterized for a particular system. For example, the implicit solvation model CPCM fails to capture the effect of water versus methanol solvents on the kinetics of the glucose hydride shift reaction.[10] This suggests that explicit solvent is required to capture mixed solvent effects on reaction kinetics.

Classical MD treats solvent molecules explicitly at much less computational expense than AIMD. To simulate solvents, an empirical force field is parameterized to reproduce bulk liquid properties such as density, heat of vaporization, and solvation free energies.[13−15] It is therefore advantageous to employ classical MD to model solvent coordinates, though a quantum description of the reaction coordinates is still required. This motivates the combination of DFT with classical MD to describe the reaction coordinates and solvent coordinates, respectively.

Quantum mechanical/molecular mechanical (QM/MM) methods combine these two approaches. QM/MM approaches typically embed a QM-treated region inside a force-field-treated extended solvent, running both simultaneously in a joint MD simulation.[16−19] The key challenge of the QM/MM approach is the treatment of the interactions between the QM and the MM regions.[16] The choice for this embedding treatment is non-trivial for more complex systems, such as in electrochemistry where the metallic surface complicates the electrostatics.[20] Our approach fits in the general category of QM/MM methods, though we separately perform QM (DFT) analysis of the reaction coordinates, then subsequently embed it into a MM treatment of solvent interaction.

In our DFT/MD model, reaction coordinates and solvent coordinates are described by DFT and classical MD, respectively, in separate calculations. The DFT and MD simulations are connected by a thermodynamic cycle (Figure 1). The horizontal arrows in the thermodynamic cycle of

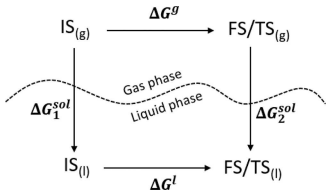

Figure 1. Thermodynamic cycle depicting a reaction or activation free energy change in the gas (ΔG^g, top) and solution (ΔG^l, bottom) phases.

Figure 1 indicate either a reaction free energy or activation free energy, depending on whether the right hand side is a final product state or a transition state. The vertical arrows indicate the solvation free energies of the initial and final/transition-state species.

The core idea of our DFT/MD approach is simple. First, DFT together with thermal corrections are used to calculate the gas-phase free energy change. This is done by geometrically optimizing the reacting species to local energy minima, corresponding to metastable reaction intermediates, or to saddle points, corresponding to transition states. The reaction initial state, intermediates, and the transition state are carried over to a separate classical MD simulation, where their solvation free energies are calculated. Finally, the solution-phase reaction/activation free energy can be computed by completing the thermodynamic cycle (eq 1).

$$\Delta G^{l} = \Delta G^{g} + \Delta G_1^{sol} - \Delta G_2^{sol} \quad (1)$$

This DFT/MD approach differs from embedded QM/MM approaches in that the DFT-treated reaction coordinates are static in the force-field MD simulation of solvation effects. Though DFT and MD simulations are run separately, there exists an intimate connection between the quantum and classical models through the DFT-assisted parameterization of the force field as will be outlined in the Methods section. This parameterization parallels the choices made in QM/MM schemes, but is simplified by the assumption that the DFT region remains frozen during our solvation simulation. This sequential procedure for integrating DFT and classical MD has also been developed previously for liquid/solid interface studies.[21,22]

Our DFT/MD model offers two major advantages over current state-of-the-art QM/MM and AIMD approaches: lower computational cost and the ability to discern solvation effects by explicitly computing the solvation free energies. Both topics will be further discussed in the Method and Result and Discussion sections.

Aprotic Co-Solvent Effect on Alcohol Dehydration Kinetics. We illustrate and validate our DFT/MD approach by studying the effect of aprotic co-solvents on the kinetics of solution-phase acid-catalyzed alcohol dehydration. Though the dehydration reaction mechanism is well known, the influence

https://doi.org/10.1021/acscatal.2c03978
ACS Catal. 2022, 12, 13193−13206

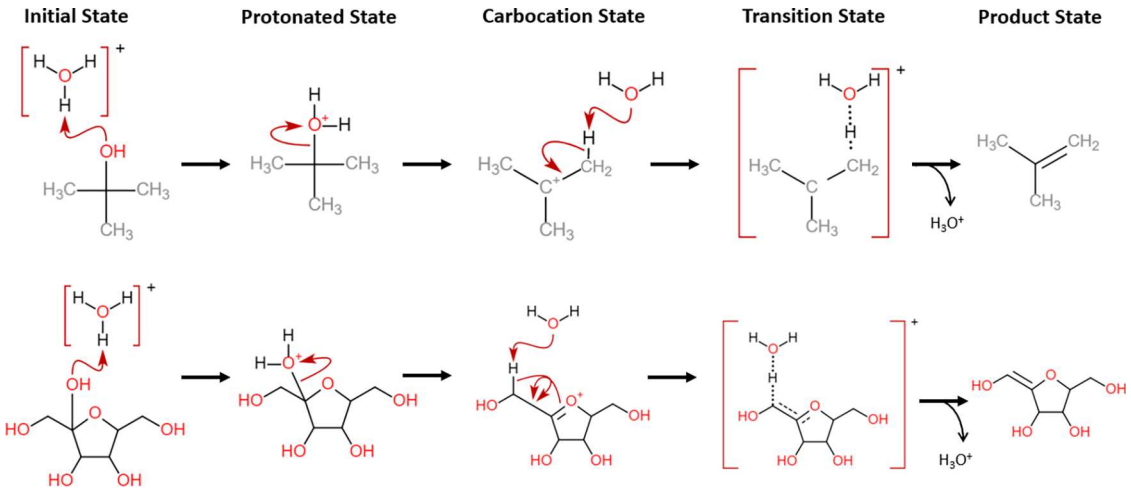

Figure 2. Cartoon depiction of the E1 dehydration mechanism on *t*-butanol (top) and fructose (bottom).

of water/organic solvent mixtures on reaction energetics was only recently investigated using AIMD simulations.[7,8,23,24] The dehydration reaction, which removes a hydroxyl group, is an ubiquitous step in the network of biomass upgrading reactions.[1] The Dumesic lab recently published extensive experimental rates for these biomass dehydration reactions, highlighting the effect of co-solvents on the reaction kinetics.[5,6,9] Their pioneering work, combined with AIMD studies done in collaboration with their experiments, provide an excellent benchmark for validation of our DFT/MD approach.

We leverage the findings from two papers by Mellmer *et al.*,[6,9] including both experimental rate measurements and AIMD activation barrier calculations performed by the Neurock lab. Experimentally, they measured the rate constants for *t*-butanol and fructose dehydration reactions in different weight ratios of water mixed with dimethylsulfoxide (DMSO), acetonitrile (MeCN), or γ-valerolactone (GVL). The reaction rate varies by 3 orders of magnitude, depending on co-solvent identity and concentration (see Figure 1 in ref 6). AIMD simulation with enhanced sampling of the reaction coordinates was used to simulate the reaction mechanism and calculate the apparent activation barriers for *t*-butanol and fructose acid-catalyzed dehydration in pure water, water/DMSO, and water/GVL. The calculated apparent activation barriers agree well with the trend of experimental rate constants. We use as benchmark from their work both the AIMD-calculated absolute apparent activation barriers, and the relative apparent activation barriers as obtained from experimental ratio of rate constants.

In summary, we apply our DFT/MD approach to calculate the activation free energies of acid-catalyzed dehydration of two biomass model alcohol molecules (*t*-butanol and fructose) in three mixed solvent systems (water with DMSO, MeCN, and GVL). The DFT/MD results are compared to both the experimentally measured rate constants and AIMD-calculated apparent activation free energies.[6,9]

DFT/MD Method. Details of the combined DFT and classical MD approach are presented below in two sections. First, specifics for the gas-phase DFT calculation of the reaction coordinates are introduced. Second, we give details for the classical MD solvation simulations, including the force-field parameterization and thermodynamic integration.

DFT Modeling of Reaction Coordinates. Molecular DFT calculations were performed using Gaussian09 software.[25] The split-valence basis set with polarization and diffuse functions 6-311G++(d,p) was used with the b3lyp[26] hybrid functional. Dehydration of both *t*-butanol and fructose follows the well-known E1 elimination mechanism (Figure 2).

The reaction coordinates were "scanned" by performing constrained optimizations. Each scan gave DFT energy minima or maxima, from which geometries were extracted and re-optimized to a reaction intermediate or a transition state, respectively, using the Berny optimization algorithm.[27] The ground-state energies of the optimized reaction states were corrected for thermal enthalpies and entropies using standard ideal gas statistical thermodynamics treatment with harmonic vibrator and rigid rotor approximations. Anharmonic vibrations may contribute to the computed gas-phase free energy, especially for the transition state with "softer" vibrations, though are not considered in our current model. The temperatures used for thermal correction were 363 K for *t*-butanol dehydration and 373 K for fructose dehydration. The DFT calculations that had a net positive +1 charge did not require a counter charge for neutrality because atomic orbital basis set was used. Details of the reaction scans can be found in Section S2 of Supporting Information.

Although we do not rely on implicit solvation models to obtain solvation free energies, we use them to stabilize the charged reaction states and relax their geometries. For this purpose, we turned on the implicit solvation model IEFPCM[28] during the reaction scans and subsequent geometry optimization of each reaction states. The gas-phase DFT energy and thermal corrections were then obtained from single-point calculations with the implicit solvation model turned off.

The gas-phase translational entropy and therefore free energy of each reaction state depends on the choice of standard-state concentration. The initial state of both alcohol reactions (Figure 2) includes the proton carrier catalyst and the alcohol molecule, each at their standard concentrations. Subsequent reaction states are "merged" structures that can be considered as one individual species. Following conventional reaction thermodynamic practice, the concentrations of all reaction species in the solution phase are chosen to be 1 M.

Solvation Free Energies Using Classical MD. Each DFT-optimized intermediate- and transition-state structure was inserted to a classical MD simulation, where thermody-

https://doi.org/10.1021/acscatal.2c03978
ACS Catal. 2022, 12, 13193−13206

namic integration[29−31] was used to calculate its solvation free energy. Thermodynamic integration is well-established and commonly used to calculate solvation free energies of small molecules, with good agreement with experiment.[32,33]

Classical MD simulations were run using GROMACS 5.1 software.[34−39] The OPLS-AA force field[40] was used with the TIP3P[41] model of water. An MD solvation run includes the solute, water solvent, and co-solvents (DMSO, MeCN, or GVL) in a cubic box of side length 3.3 nm (pure water) or 4.0 nm (mixed solvents). Considering the Bjerrum length of pure water at 298 K (373 K) is about 0.7 nm (0.5 nm), the 3.3 nm box length is then adequate to screen the electrostatic interaction between the charged solute and its periodic image. The Bjerrum length is expected to increase with the addition of aprotic co-solvent that has a lower dielectric constant, which motivated a slight increase of box length to 4.0 nm. Co-solvent mixtures were packed with the solute into the simulation box using Packmol software.[42] The system equilibrated using 5000 steps of steepest descent minimization followed by two short NVT and NPT runs of 100 ps each. The production run time is 8 ns per λ value (total of 29 λ values), where λ is the thermodynamic integration parameter that tunes the interactions between the reaction states and the solvents. The run time was chosen to be long enough to obtain a reasonably smooth curve as shown in Figure 10 (simulation time convergence tests are shown in Section S6 of Supporting Information). A time step of 2 fs was used with the SETTLE[43] treatment of water molecules. The temperatures were thermostatted using velocity rescaling,[44] to experimental values:[6] 363 K for *t*-butanol and 373 K for fructose. The Berendsen barostat[45] was used with a pressure of 1 bar. A background homogeneous −1 charge cancels the +1 positive charge on the reaction states.

The force-field parameters for co-solvent molecules (DMSO, MeCN, and GVL) were tuned to reproduce experimental enthalpies of mixing with water. Details of the parameters and tuning are reported in Section S1 of Supporting Information. This tuning ensures a thermodynamically accurate solvation environment before embedding and solvating any reaction state.

The choice of force-field parameters for the reaction states is non-trivial because reaction intermediates and transition states cannot be represented by default force-field parameters intended for stable molecules. This model choice is critical as it dictates the strength of interaction of each reaction state with the solvents.

Non-bonded interactions include electrostatic interactions, parameterized by the atomic partial charges, and dispersive interactions, parameterized by the Lennard-Jones 6−12 parameters. The Lennard-Jones parameters of a reaction state are taken from default OPLS-AA parameters because the atomic rearrangements during a reaction step are unlikely to significantly alter the electronic polarizability of the atom constituents. In contrast, the partial charges are adjusted at each reaction step because the electronic dipole and monopoles change quite significantly along the reaction coordinate. We used the electrostatic potential fitting (ESP) method[46,47] in DFT (with continuum solvation turned off) to determine the atomic partial charges, which were then employed in the force-field MD simulations. Full tables of non-bonded parameters for the reaction states can be found in Section S3 of Supporting Information.

Bonded interactions within the "solute" reaction states are not included because their internal coordinates are frozen during MD simulations. This simplification has several advantages. First, we avoid having to develop the parameters for numerous internal degrees of freedom. Second, the transition state is a saddle point in the potential energy surface and would require artificial stabilization of the unstable mode. Though one may argue that the relaxation of the internal coordinates of the solute significantly contributes to its solvation free energy, by treating all reaction states as frozen, we expect reasonable error cancellations because we ultimately only need relative solvation free energies in different solvents for our predictions (eq 1). In Section S5 of Supporting Information, we lay out several calculations for the hydration free energies of small organic molecules and charged proton-water clusters with and without the frozen solute treatment to assess the degree of error cancellation.

Classical MD is far less computationally expensive compared to AIMD, allowing for much better sampling of solvent configurations. For example, consider the system of 90 wt % DMSO. Our classical MD simulation consists of 450 DMSO and 210 H_2O molecules, which runs 52 ns per day using four CPUs with one GPU. With tractable computing resources, our classical MD can easily afford nanoseconds of solvent equilibration around the reactive centers, which we found necessary to obtain a statistically converged relative solvation free energy results (see Section S6 of Supporting Information). AIMD simulation of the same 90 wt % DMSO system, reported by Mellmer *et al.*, used 21 DMSO with 10 H_2O molecules,[6] which ran for only 20 picoseconds at each collective variable window. By comparing with a system of 64 water, which has roughly the same number of valence electrons, we estimate such an AIMD simulation runs for 0.014 ns per day using 28 CPUs.

Though less extreme than AIMD, in the QM/MM approach, dynamic evolution of the QM region still incurs significant computational costs. The charged reaction species along with a small number of solvent molecules need to be included in the QM region to have realistic short-range interactions[17,19] (much like our choice of DFT-treated solvent discussed in the next section). Similar to AIMD, the reaction coordinates in the QM region need to be sampled along some path defined by a collective variable using umbrella sampling or metadynamics.[11] The sampling of each collective variable window then needs to be long enough to allow for solvent reconfiguration in the MM region.

We highlight that 8 ns/λ × 29λ = 232 ns of dynamic simulation was needed to obtain reliable statistics for solvation of a single intermediate or transition state for a single (mixed) solvent using classical MD. We report here activation free energies for 67 combinations of reactions and solvents, requiring collectively over 31,000 ns of dynamic simulation. To run AIMD or QM/MM dynamics for this length of simulation time (with 0.5 fs time step) would require 5.6 billion energy/force evaluations. This is orders of magnitude beyond what is viable using AIMD or QM/MM simulations.

Finally, a major benefit of explicitly computing the solvation free energies is that it provides a clear indicator for the solvation impact on reaction energetics, something not attainable from conventional enhanced sampling using QM/MM or AIMD simulations. The potential of mean force obtained from enhanced sampling of any reaction coordinate is always relative to an arbitrary starting point within that

https://doi.org/10.1021/acscatal.2c03978
ACS Catal. 2022, 12, 13193−13206

particular coordinate. This means that though one may attain a lower activation barrier for a particular reaction by changing from solvent A to solvent B, one cannot immediately tell if solvent B is destabilizing the initial state or stabilizing the transition state (or both) relative to solvent A because there is no common starting point between the two solvents. In contrast, our DFT/MD model computes the solution-phase reaction free energy profile with a common starting point: the gas-phase free energy. By computing the solvation free energies of all the reaction intermediates and the transition state into solvent A or B from the same gas-phase reference, our model allows for an immediate assessment of the solvation role on the change in activation barrier. We later illustrate this improved interpretability of solvation effects in Figure 11.

Choice of DFT-Treated Proton Carrier. Though the classical MD simulation is used to quantify solvation, nearby solvent molecules can directly alter the reaction coordinates,[8] which requires a DFT description. The solvent interactions can be separated into short-range electronic and longer range electrostatic effects. The short-range electronic effect describes how nearby solvent molecules impact the local electron densities around the reaction states. These short-range solvent molecules should be included in the static DFT region. Conversely, the longer range electrostatic effect includes both medium range interactions such as dispersion, dipole−dipole or hydrogen bonding, and also longer range dielectric screening. These electrostatic interactions can be well described by the classical force field. The question is, therefore: how does one decide to use DFT or force field to treat a given solvent molecule?

Answering this question requires a chemical understanding of the reaction coordinates, as well as some testing. In this section, we present a simple test using the DFT/MD approach to determine which and how many solvent molecules should be included in the DFT model.

Which Solvents Act as Proton Carriers? We first address which solvent in a mixed system acts as the proton carrier and thus should be included in the DFT region. In pure water at room temperature, we expect the proton carrier to be the Zundel cation, $H_5O_2^+$, a structure known to facilitate proton transfer in aqueous solution.[48−53] In mixed solvents, the aprotic co-solvent could either take over or assist water in stabilizing the excess proton.

To decide the choice of which proton carrier to use for each co-solvent system, we compute the proton transfer free energy between proton clusters, using the DFT/MD framework with the thermocycle as shown in Figure 3. In this way, we calculate ΔG^{l}_{PT}, the free energy change to transfer the proton from a protonated water cluster to a protonated co-solvent cluster at 373 K, an elevated temperature relevant to the reactions in this study. The solvation of each species was done in liquid water. The standard concentration of water is 55 M and that of A or A−H_3O^+ is 1 M. Figure 4 summarizes results of ΔG^{l}_{PT} for each aprotic co-solvent.

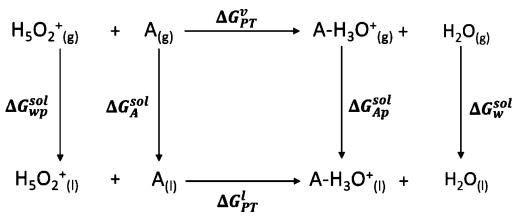

Figure 3. Thermodynamic cycle for the proton transfer between water and aprotic solvent molecules. Species A depicts any aprotic co-solvent molecule in consideration: DMSO, MeCN, and GVL. The solvation free energies are computed in pure water.

All aprotic co-solvents were found to thermodynamically prefer to assist water instead of completely taking over the proton carrying task (*i.e.*, A−H_3O^+ instead of A−H^+ or A−H−A^+, see Section S8 of Supporting Information). From the values of ΔG^{l}_{PT}, it is evident that in solution, the order of favorability for carrying the excess proton is: DMSO−H_3O^+ > $H_5O_2^+$ > MeCN−H_3O^+ > GVL−H_3O^+.

Based on pKa values[54] of protonated acetonitrile (−10.1), protonated GVL (−7.0 for protonated ester), and protonated water (−1.74), we expect that the excess proton readily resides only on water molecules for water/MeCN or water/GVL mixtures at room temperature. The large values of ΔG^{l}_{PT} for MeCN and GVL indicates that the population of MeCN−H_3O^+ and GVL−H_3O^+ is negligible except for at very high concentration of the respective aprotic co-solvents. This result suggests that the proton carrier taking part in the dehydration reaction (Figure 2) is $H_5O_2^+$ for both water/MeCN and water/GVL mixtures.

In contrast, DMSO readily shares the excess proton with water. The proton affinity of the oxygen bonded with the sulfur in DMSO is significantly larger than the nitrogen on MeCN or the oxygen on GVL. This is apparent from the pKa value of protonated DMSO (−1.80),[54] being comparable to that of water. Furthermore, simulations and spectroscopic experiments have confirmed the formation of the DMSO−H_3O^+ complex in water/DMSO mixtures.[6,55,56]

Though the thermodynamic stability of DMSO−H_3O^+ over $H_5O_2^+$ is apparent and would suggest modeling the proton carrier as DMSO−H_3O^+ in the reaction coordinates, we instead still choose to use $H_5O_2^+$ as the proton carrier in water/DMSO mixtures, following further analysis on the reaction free energy profile. Figure 5 shows the free energy of protonating a *t*-butanol molecule using either $H_5O_2^+$ or DMSO−H_3O^+, as calculated in pure water solvent using DFT/MD.

The result in Figure 5 suggests that, though DMSO−H_3O^+ is more stable in the bulk solvent, the proton donor in contact with *t*-butanol is preferred as $H_5O_2^+$. This is consistent with the benchmarking AIMD simulation in ref 6 where the excess proton approximately retains a $H_5O_2^+$ structure in close proximity with the *t*-butanol reactant even at 90 wt % DMSO. We will compare our activation barriers to these AIMD results, where the initial state is referenced to the excess proton in the vicinity of the alcohol reactant; therefore for consistency, we model the proton carrier as $H_5O_2^+$ in the water/DMSO mixture.

How Many and Where Are the Proton Carriers? With the decision to use water as the proton carrier for all mixtures, we now must choose how many and where to place the water molecules within the DFT representation. In the dehydration reaction coordinates, the protonated water cluster initially acts as a proton donor and then acts as a proton acceptor when the proton is transferred from the carbocation (see Figure 2). Figure 6 shows an example of two water molecules acting as the proton donor, while two acting as the proton acceptor.

The solvent molecules circled in Figure 6 require a DFT description if they significantly alter the electronic densities and hence the chemical potential of the reaction states. We aim to include the least number of solvent molecules in the DFT representation because: (1) force-field dynamic simulation of

https://doi.org/10.1021/acscatal.2c03978
ACS Catal. 2022, 12, 13193−13206

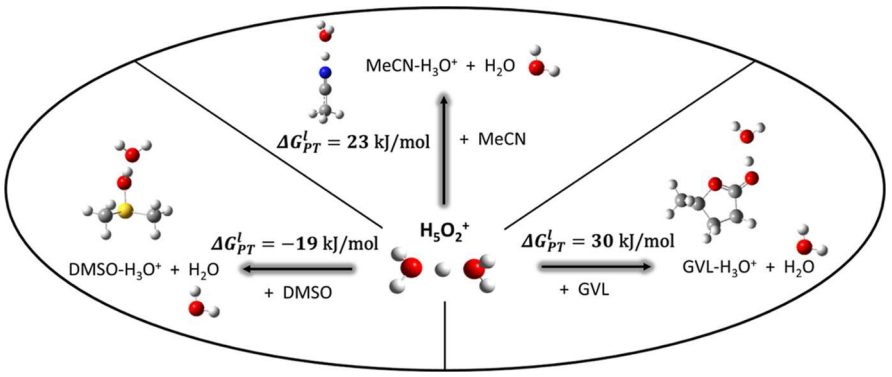

Figure 4. queous-phase free energy transfer of the excess proton from $H_5O_2^+$ to the most stable form of proton carrier for each respective aprotic co-solvent (DMSO, GVL, and MeCN).

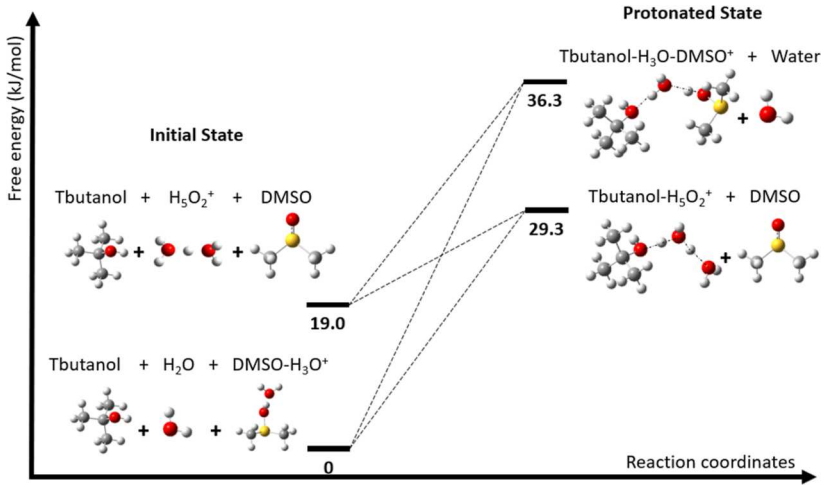

Figure 5. Free energy change of the first protonation step for *t*-butanol, using either $H_5O_2^+$ or DMSO−H_3O^+. The initial state depicts each reactant in bulk solution at its reference concentrations. The protonated state depicts bringing the proton carrier in close proximity with the *t*-butanol molecule and sharing the proton with its oxygen.

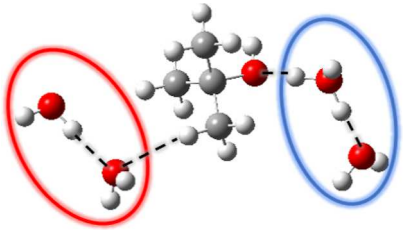

Figure 6. DFT-optimized protonated state for *t*-butanol dehydration. The $H_5O_2^+$ structure circled on the right will donate the proton in the first protonation elementary step. In the last deprotonation step, the two water molecules on the left will accept the proton from the methyl group to generate the alkene and reform an $H_5O_2^+$ cluster.

these molecules is much less computationally expensive and (2) only tightly bound solvent molecules at a given state are properly represented as static, with their entropy contribution removed. This entropy penalty may exceed the energy (enthalpy) benefit of being included in the DFT cluster, making the addition of a solvent molecule to the DFT region thermodynamically unfavorable.

We show in Figure 7 the free energy change to reach the first protonation step in pure water, with different choices for the initial protonated water cluster (H_3O^+*vs* $H_5O_2^+$) and varying the number of water molecules included in the DFT representation of the alcohol-proton-water cluster.

We first look at placing water molecules as the proton donor for *t*-butanol. With three water molecules to use, the proton donor can be H_3O^+, $H_5O_2^+$, or $H_7O_3^+$. Although adding additional water always lowers the enthalpy, there is also an entropy loss associated with requiring a water molecule to be static. As seen from the bottom three protonated scenarios in Figure 7, protonating *t*-butanol with $H_5O_2^+$ incurs the least free energy cost (10.6 kJ/mol). Relative to the *t*-butanol-$H_5O_2^+$ cluster, *t*-butanol-H_3O^+ pays an enthalpic penalty larger than the entropy gain from removing one static water and hence is 14.0 kJ/mol less stable (in free energy). In contrast, adding another water to *t*-butanol-$H_5O_2^+$ and making *t*-butanol-$H_7O_3^+$ incurs a net free energy cost of 4.2 kJ/mol, stemming from the loss in entropy that outweighs the enthalpic benefit. Furthermore, H_3O^+ in bulk solvent is also not as thermodynamically stable as $H_5O_2^+$, as seen from the 12.8 kJ/mol difference in the initial state. The thermodynamic of the excess proton in solution is itself a non-trivial topic, of which was studied in our previous work.[57]

Turning to the proton acceptor for the last protonation step, the top right state in Figure 7 depicts adding an extra flanking water molecule, ready to accept the methyl proton. The entropy loss of holding the flanking water static far outweighs the enthalpy gain from stabilizing the proton on a $-CH_3$

https://doi.org/10.1021/acscatal.2c03978
ACS Catal. 2022, 12, 13193−13206

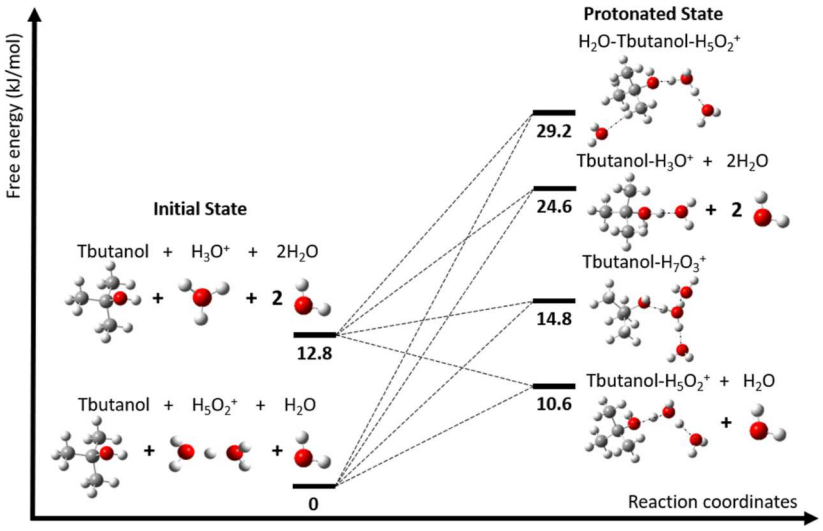

Figure 7. Free energy change of the first protonation step for *t*-butanol with different placement of water molecules.

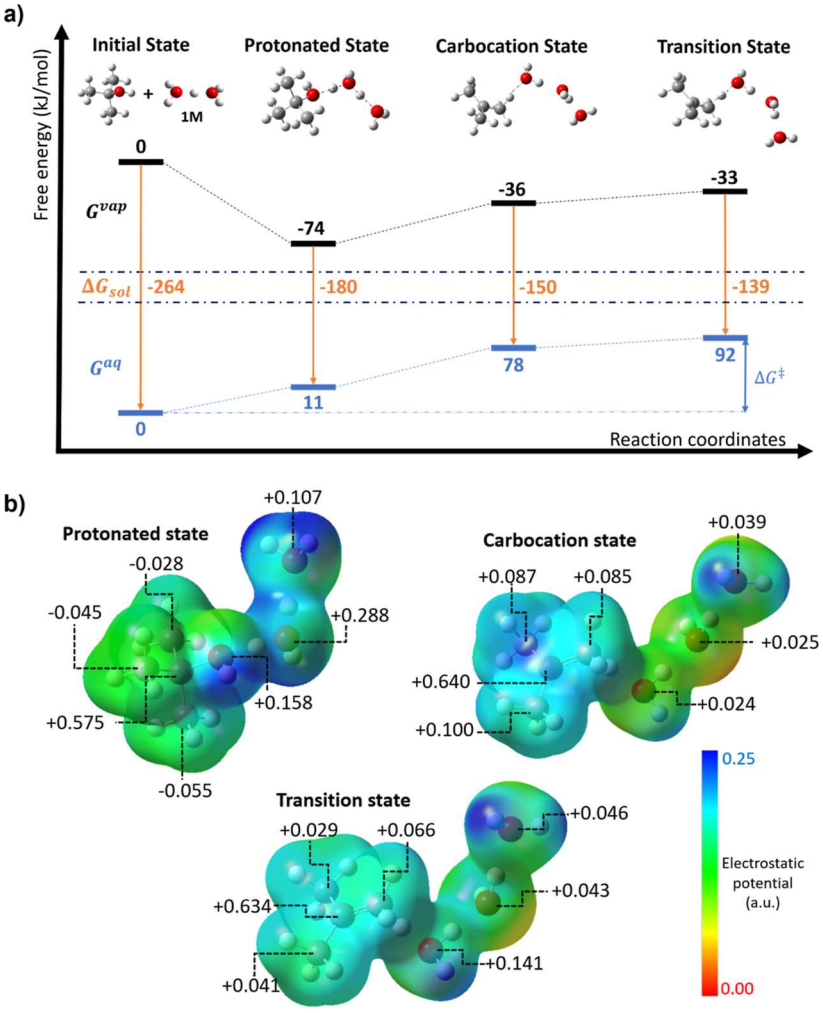

Figure 8. (a) Reaction free energy profile of *t*-butanol dehydration in the gas phase (top) and in water solvent (bottom), each profile referenced to its respective initial state. The solvation free energies of each reaction states are shown in the middle section. The activation free energy $\Delta G^{\ddagger}$ is the free energy difference between the solvated transition and initial states. Each reaction state corresponds to the elementary steps shown in Figure 2. (b) Electrostatic potential iso-surface around the reaction states, with labels for the ESP charges of the heavy atoms (C and O) plus neighboring H atoms. The +1 charge is more localized among the oxygens in the protonated state, among the carbons in the carbocation state, and smeared out to all carbons and oxygens in the transition state.

https://doi.org/10.1021/acscatal.2c03978
ACS Catal. 2022, 12, 13193−13206

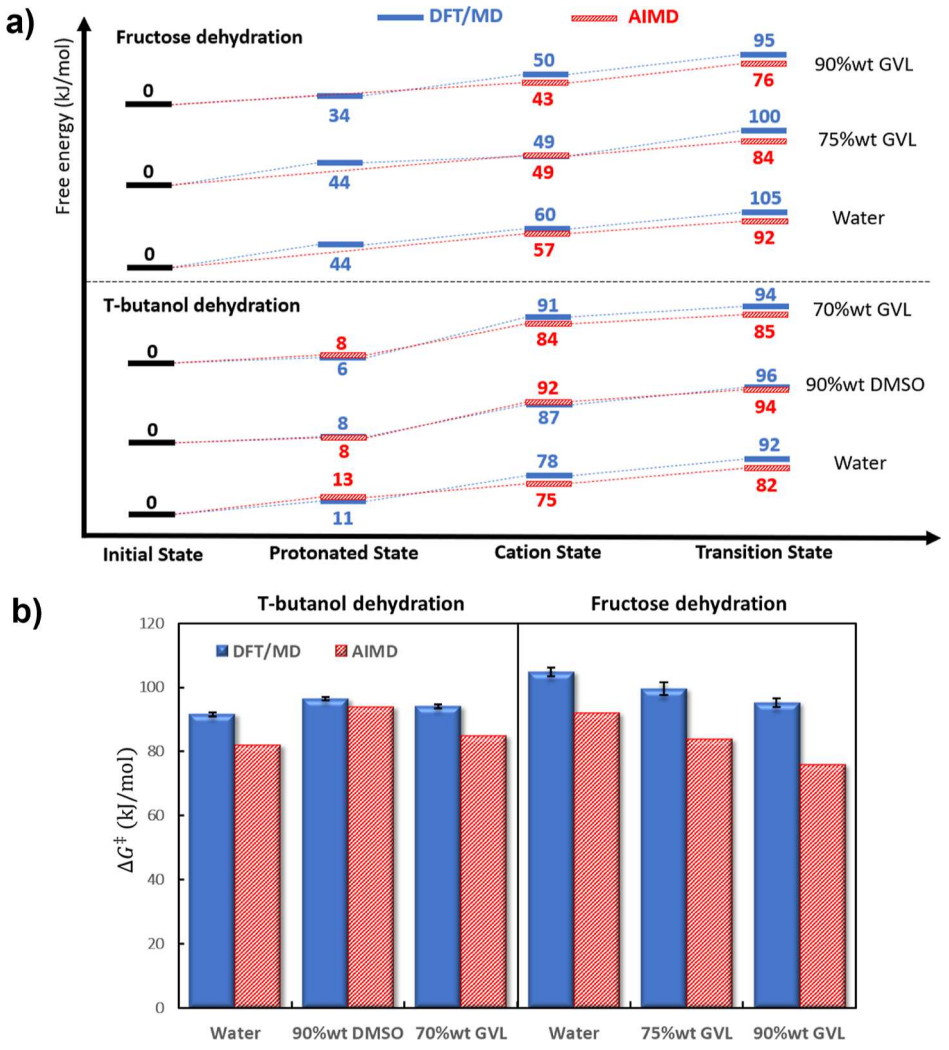

Figure 9. (a) Reaction free energy profile of *t*-butanol (bottom) and fructose (top) in various solvents. DFT/MD profile shows reasonable agreement with AIMD's across the board. (b) Comparison of activation free energies of above reactions from DFT/MD versus AIMD. DFT/MD's barriers are consistently slightly larger, but follow AIMD's trend closely. AIMD results were taken from refs 6 and 9.

group, incurring a net free energy cost of 18.6 kJ/mol. Furthermore, the water molecules acting as the proton donors in the first protonation step can serve as the proton acceptors in the last deprotonation step (Section S2 of Supporting Information).

Altogether, the results in Figures 4, 5, and 7 guide us toward choosing to simply use two water molecules as both the proton donor and proton acceptor along the reaction coordinate in all solvent mixtures. On reflection, these are not difficult choices, at least when considering mixed water/MeCN and water/GVL solvents. Water clusters will carry the proton and serve as the proton donor to the alcohol and acceptor to the methyl proton. Two water molecules benefit from significant enthalpic interaction with the positive charge along the reaction coordinate, such that they can be treated statically. By carefully studying how DFT-treated solvent molecules affect reaction energetics within our DFT/MD framework, we obtain valuable information about the balance of enthalpy/entropy contributions to solvation.

DFT/MD Energetic Results. *Reaction Free Energy Profile.* With the choice of proton carrier made, we map the free energy profile for the intermediates and the transition state in the alcohol dehydration mechanism. Figure 8a illustrates the reaction free energy profile calculated in the gas phase using DFT and solvated to the aqueous phase using MD. In the aqueous phase, the difference in free energies of the transition state and initial state gives the activation free energy $\Delta G^{\ddagger}$ of 92 kJ/mol in pure water solvent.

The first protonated step in the gas phase is downhill in free energy. This is because in the gas phase, the excess +1 charge on the $H_5O_2^+$ species favors the stabilization provided by the *t*-butanol molecule. After solvating the initial state into liquid water, the excess positive charge is largely stabilized by dielectric screening of the solvent. Furthermore, bringing the solvated $H_5O_2^+$ to protonate a *t*-butanol molecule requires giving up a water molecule hydrogen-bonded to the $H_5O_2^+$ cluster, incurring a net free energy cost of 11 kJ/mol. In other words, the net solvent stabilization of separated *t*-butanol and $H_5O_2^+$ species (−264 kJ/mol) outweighs their interaction (−74 kJ/mol) plus the solvation of the protonated state (−180 kJ/mol).

In subsequent reaction states, the C−O bond is first cleaved to produce a carbocation, then a proton hops from a $-CH_3$ group onto water molecules. The gas-phase free energy profile for this sequence is an uphill activated process. Once the protonated state is formed, it would require 41 kJ/mol to

https://doi.org/10.1021/acscatal.2c03978
ACS Catal. 2022, 12, 13193−13206

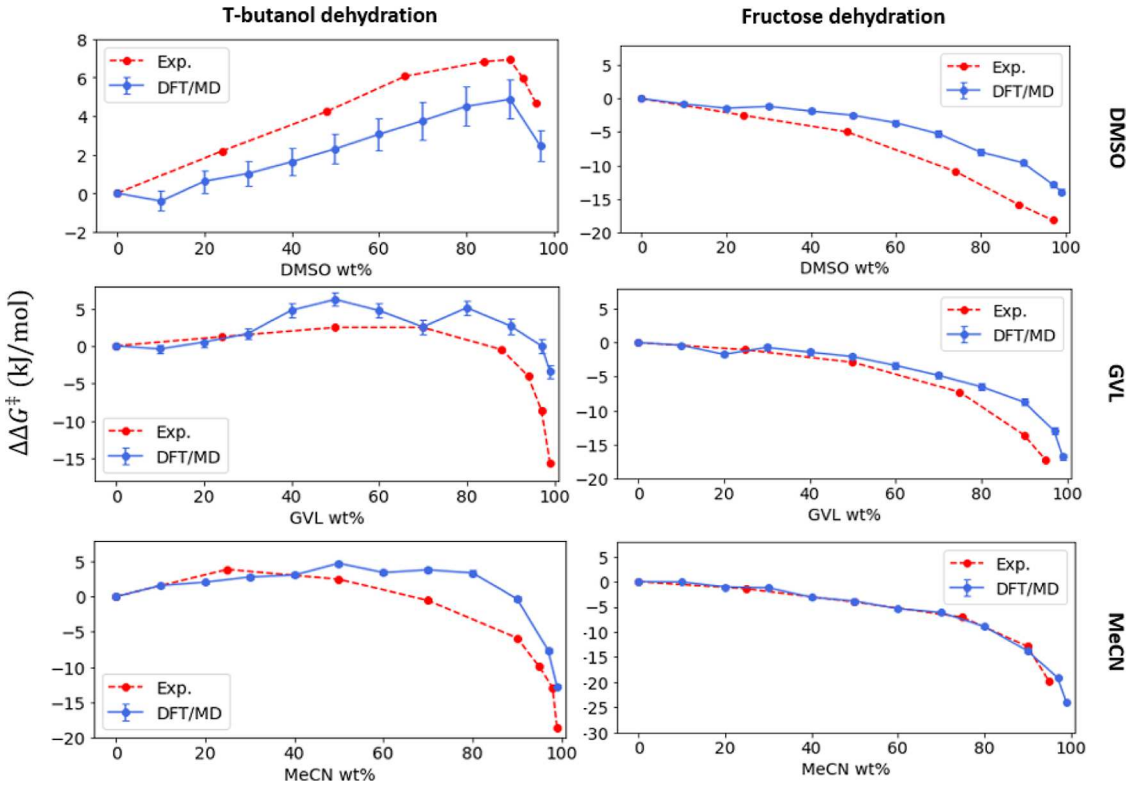

Figure 10. Relative activation free energies ($\Delta G^{\ddagger}_{mix} - \Delta G^{\ddagger}_{w}$) of the *t*-butanol (left) and fructose (right) dehydration reaction in water/DMSO, water/GVL, and water/MeCN.

overcome the free energy barrier to complete the reaction in the gas phase (difference in gas-phase transition and protonated states in Figure 8a). The same activated process requires 81 kJ/mol in the aqueous phase. This increased free energy cost stems from the decrease in solvation free energy as the reaction progresses (see ΔG_{sol} in Figure 8a).

The decrease in solvation free energies along the reaction path can be explained from the delocalization of the excess +1 charge (Figure 8b). As the nuclei rearranges along the reaction path, the +1 charge first localizes on the three H_2O proton carriers, then on $C_4H_9^+$ carbocation, and finally delocalizes throughout the transition state. The "smeared-out" positive charge electrostatically interacts less strongly with polar solvent molecules, ultimately reducing its solvation free energy. Within the DFT/MD framework, this electronic delocalization is captured when the atomic partial charges of the reaction states are obtained from the ESP scheme in DFT calculations (Figure 8b).

The acid concentration, which governs the translational entropy of the excess proton, affects the activation free energy (Section S4 of Supporting Information). As the concentration increases, the translational entropy of the proton decreases, consequently increasing the chemical potential of the initial state and lowering the activation free energy; at higher acid concentration, it is "thermodynamically easier" for the *t*-butanol molecule to find an excess proton to react with. Below when we compute the activation free energies in mixed solvents, we use 1 M acid standard concentration, consistent with common practice in reaction thermodynamics literature.

Absolute Activation Barrier versus AIMD. We compute the free energy profile along the reaction coordinates for the dehydration of *t*-butanol and fructose in pure water and in water/organic co-solvent mixtures, as shown in Figure 9a. The mixed solvent compositions are chosen to match previous AIMD studies of the same reactions in refs 6 and 9. The activation free energies are again plotted in Figure 9b for in-scale comparison between DFT/MD (with statistical error bars from MD simulation) and AIMD.

As seen from Figure 9a, the agreement of the free energy profiles between DFT/MD and AIMD is rather impressive, especially given significant differences between approaches. The AIMD free energy profiles were obtained from umbrella sampling using a pre-determined set of collective variables.[6,9] This approach samples the collective variables under a biased force, allowing for a weighted histogram analysis method implementation. Ultimately, its accuracy relies on the calculations of the atomic forces performed by DFT at each MD time step, which capture both the reaction and solvent coordinates together. In contrast, the DFT/MD approach completely decouples the gas-phase reaction free energy and the solvation free energy and employs a thermodynamic cycle to connect them. Aside from yielding this satisfying agreement between the two methods, this validates our earlier partition of the solvation effects between short-range electronic and longer range electrostatic contributions, which could be modeled by DFT and classical MD separately.

The comparison shown in Figure 9b indicates consistently higher activation free energies predicted by DFT/MD. The trend across different solvents for both reactions, however, agrees excellently between the two methods. Larger activation free energies computed in DFT/MD could stem from our chosen 1 M acid standard concentration, and furthermore point to one subtle difference between the AIMD and DFT/MD approaches. As eluded to earlier in the analysis of Figure 5,

https://doi.org/10.1021/acscatal.2c03978
ACS Catal. 2022, 12, 13193−13206

the AIMD free energy profile is referenced to an initial state where the proton carrier is already close to the biomass molecule. Whereas, the DFT/MD free energy profile references a proton carrier solvated in the bulk at some chosen standard concentration. As well known[6,7,56] and also shown later, mixed solvent configurations in the bulk are very different to those in local proximity with a charged solute. This gives rise to an "effective concentration" of the proton in the local environment of the reaction state that is non-trivial to predict. We suggest that this different initial state free energy reference of the proton is the cause of the consistent deviation in the activation free energies calculated by the two methods as shown in Figure 9b. The direction of this difference is appropriate, as we find a free energy increase to bring the bulk proton carrier toward the alcohol molecule, and the AIMD free energy profile[6] also shows this increase to be progressive as the proton approaches the alcohol molecule. This suggests that the initial state in AIMD simulation is already slightly higher in free energy than a true bulk initial state, leading to lower AIMD-measured activation free energies.

Besides producing remarkably similar energetics compared to AIMD, the DFT/MD method does so with significantly lower computational cost. DFT calculations are needed for only gas-phase reaction scans, while classical force field provides excellent sampling of solvent configurations. Well-sampled solvent configurations also allow for meaningful statistical error bars, which can be made more precise simply by running longer MD simulations with tractable cost.

Relative Activation Barrier versus Experiment. We next compare our calculated activation free energies to experimental rate constants from ref 6, The data presented in ref 6 consists of the ratios of reaction rate constants in mixed solvent to that in pure water k_{mix}/k_w at different water/organic co-solvent compositions. Employing classical transition state theory, we transform the ratio of rate constants into the relative activation free energy

$$\Delta\Delta G^{\ddagger} = \Delta G^{\ddagger}_{mix} - \Delta G^{\ddagger}_{w} = -RT \ln \frac{k_{mix}}{k_w} \quad (2)$$

The dependence on acid concentration cancels in the calculation of the free energy difference. The experimentally inferred relative activation free energy $\Delta\Delta G^{\ddagger}$ is directly comparable to that computed from DFT/MD.

The relative activation free energies are plotted in Figure 10 for both *t*-butanol and fructose dehydration in water/DMSO, water/MeCN, and water/GVL solvents. Good quantitative agreement is observed across the board. For the *t*-butanol reaction, the slight positive values in $\Delta\Delta G^{\ddagger}$ (*i.e.*, elevated activation barrier) by adding moderate amount of MeCN or GVL, followed by a dip to negative values at very high co-solvent concentration (>80 wt %) are observed. In contrast, the fructose dehydration activation free energies consistently decrease with addition of any aprotic co-solvent. This good agreement of our results with experimental rate measurements further validates the DFT/MD approach.

As unique to our DFT/MD approach, we can interpret the change in the activation free energy across different solvents directly from the change in solvation free energies of the initial and transition states. This idea is illustrated in Figure 11. The initial and transition states of both *t*-butanol and fructose

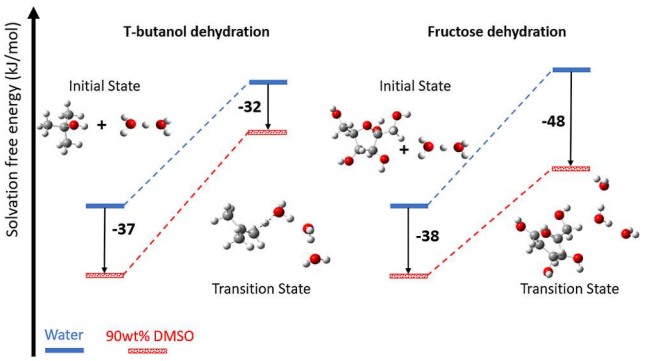

Figure 11. Change in solvation free energies of *t*-butanol (left) and fructose (right) initial and transition states from water to 90 wt % DMSO.

reactions are stabilized from the addition of DMSO to water. This is a general trend for MeCN/water and GVL/water mixtures as well (see Section S7 in Supporting Information). The difference in solvation free energies between the initial and transition states explains the change in activation free energies. For *t*-butanol dehydration, 90 wt % DMSO, relative to water, stabilizes the initial state 5 kJ/mol stronger compared to the transition state, giving rise to the observed 5 kJ/mol increase in the activation free energy. The reverse is true for fructose dehydration, having a 10 kJ/mol lower activation free energy at 90 wt % DMSO. We stress once again that the conventional enhanced sampling of reaction coordinates used in AIMD and other QM/MM approaches cannot provide such solvation comparison on an absolute scale as shown in Figure 11.

Mixed Solvent Structuring. The distribution of mixed solvents around the reaction states of alcohol dehydration has been considered by others. Recent work used classical MD to map out solvent distribution around the biomass reactant[7,12,58] or around the excess proton carrier.[56] MD-derived structural information was then used as descriptors for a neural network model[23] or a multivariate model.[59] These models aim to provide rapid and accurate predictions for the rate of biomass reactions in mixed aqueous/organic solvents.

Improving on these results, the DFT/MD approach captures the structuring of solvent around not only the reactant, but around metastable reaction intermediates and transition states. We characterize the solvent configurations in terms of 2D radial distribution functions (RDFs) or alternatively in more details with 3D spatial distribution functions (SDFs), obtained from 8 ns trajectory of classical MD about a DFT-determined reaction state.

Figure 12 displays the RDFs between oxygens on the transition state of *t*-butanol dehydration and oxygens on either water or DMSO. In the top figure, the water or DMSO concentrations are referenced either to pure water or 97 wt % DMSO, respectively. This figure therefore compares local solvent concentrations on an absolute scale across different solvent compositions. From this figure, it is evident that the absolute number of water (DMSO) in the local region (<0.35 nm) of the transition state goes down (up) as more DMSO is added.

In contrast, the bottom RDFs are normalized with respect to the bulk concentration of each respective solution, which allow for comparison in relative scale across solvent compositions. For both water or DMSO, the first RDF peak increases with

https://doi.org/10.1021/acscatal.2c03978
ACS Catal. 2022, 12, 13193−13206

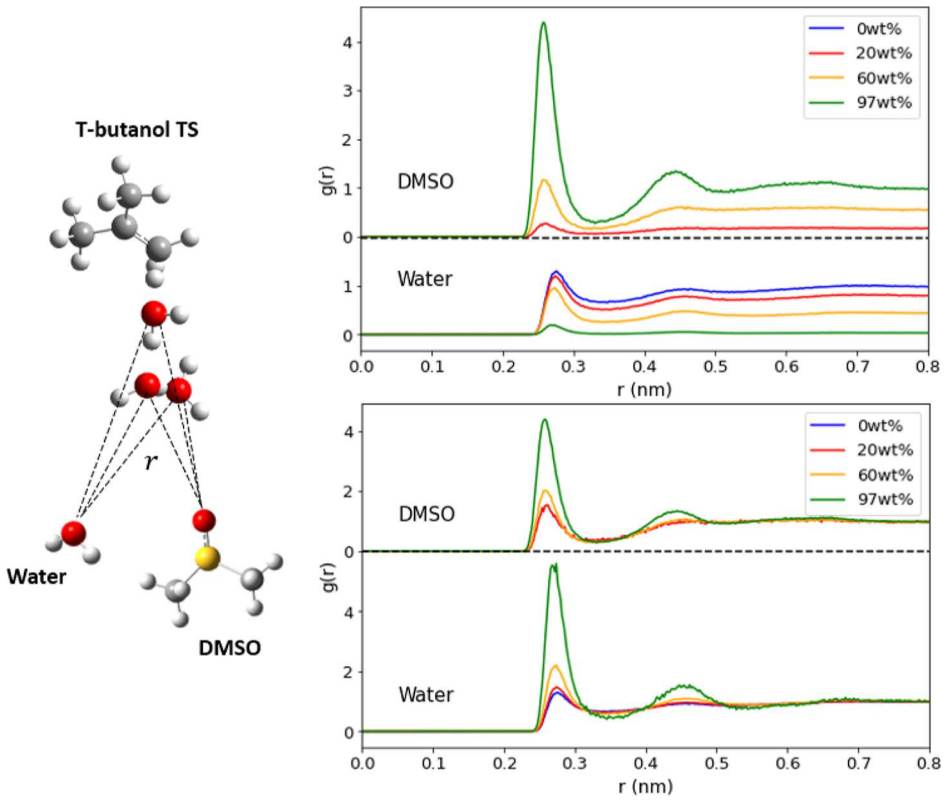

Figure 12. RDFs for oxygens on the transition state of *t*-butanol dehydration and the oxygens on water or on DMSO. The top RDFs are referenced to the bulk density of water in pure water (0 wt %) or DMSO in 97 wt % DMSO. The bottom RDFs are referenced to bulk density of the respective solution.

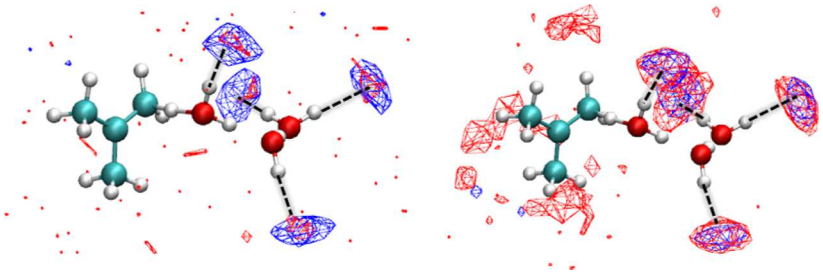

Figure 13. SDFs for oxygens on the transition state of *t*-butanol dehydration and the oxygens on water (blue) or on DMSO (red). The left and right boxes are for 20 and 97 wt % DMSO, respectively. The dashed black line indicates obvious hydrogen bonds.

higher DMSO concentration. This means that for water, though the absolute number of water molecules (per unit volume) near the solute goes down with higher DMSO concentration, the number of local water molecule relative to that in the bulk goes up. The increasing number of local molecules with respect to the bulk is also true for DMSO. This affinity of the reaction state for water versus for aprotic co-solvent is termed "preferential clustering" in previous studies of mixed aqueous/organic solvent and is used as a descriptor for a predictive model.[7,23]

Figure 13 shows the 3D SDFs for 20 and 97 wt % DMSO. It is clear that at low concentration of DMSO, the oxygens on water (blue region) and DMSO (red region) compete to form hydrogen bonds (black dashed lines) with the four free −OH groups of the transition state. At higher DMSO concentration, the DMSO molecules also flank behind the hydrophobic part of the transition state.

In summary, our solvent structural analysis confirms recently established understanding of co-solvent preferential clustering. Furthermore, most published studies of solvation effects in mixed solvent relies on analyzing solvent configurations around only the biomass reactant (*i.e.*, *t*-butanol or fructose).[7,12,56] Our DFT/MD approach provides the same structural analysis for any desired state along the reaction path. Though outside the current scope of our work, in-depth analysis of how co-solvent rearranges along the reaction path could provide new descriptors for future predictive models.

CONCLUSIONS

In this work, we have presented a DFT/MD approach to compute activation free energies for alcohol dehydration reactions in mixed solvents. The calculated activation barriers are validated by comparison to both AIMD computations and experimental rate measurements from refs 6 and 9 with excellent agreement.

https://doi.org/10.1021/acscatal.2c03978
ACS Catal. 2022, 12, 13193−13206

From this successful validation, we provide deeper understanding of solvent influence on the reaction mechanism and energetics. Solvent molecules interact with the reaction species through both short-range electronic and longer range electrostatic contribution. The short-range electronic interaction significantly alters the electronic structures of the reaction state, necessitating a DFT-level description. The longer range electrostatic interaction includes dispersion, dipole−dipole or hydrogen bonding, and long-range dielectric screening. These interactions can be well described using classical force fields in MD simulations. The solvation effect on a condensed phase reaction is therefore an interplay between these two types of interactions, and also between enthalpic stabilization and the entropy penalty of solvent molecule taking part in the reaction mechanism. Furthermore, by explicitly calculating the solvation free energies, the reaction free energy profiles can be compared across solvents on an absolute free energy scale.

Our DFT/MD approach is a very scalable procedure. The static DFT description significantly reduces the computational costs in comparison with AIMD and QM/MM approaches that dynamically sample the reaction coordinates. With careful consideration of DFT versus force-field treatments of the reaction coordinates and solvent coordinates, respectively, the approach can be extended to condensed-phase reactions with more complex mechanisms or in more complex environments such as porous solid catalysts.[2,4]

Besides computing reaction energetics, our simulation also reveals how co-solvents structure around each state of a reaction path. These data can be readily extended for various different reactions in different solvents, potentially offering valuable descriptors in recently developed predictive models for the rate of biomass reactions.

■ ASSOCIATED CONTENT

Supporting Information

The Supporting Information is available free of charge at https://pubs.acs.org/doi/10.1021/acscatal.2c03978.

Force-field parameters and DFT reaction scan profiles (PDF)

■ AUTHOR INFORMATION

Corresponding Author

Michael J. Janik − *Department of Chemical Engineering, Pennsylvania State University, University Park, Pennsylvania 16802, United States;* orcid.org/0000-0001-9975-0650; Email: mjj13@psu.edu

Authors

Bolton Tran − *Department of Chemical Engineering, Pennsylvania State University, University Park, Pennsylvania 16802, United States;* orcid.org/0000-0003-2645-4898

Scott T. Milner − *Department of Chemical Engineering, Pennsylvania State University, University Park, Pennsylvania 16802, United States;* orcid.org/0000-0002-9774-3307

Complete contact information is available at: https://pubs.acs.org/10.1021/acscatal.2c03978

Notes

The authors declare no competing financial interest.

■ ACKNOWLEDGMENTS

The authors acknowledge funding from NSF-CBET 1939464 and support from the William H. Joyce Chair. This work used the Extreme Science and Engineering Discovery Environment (XSEDE), which is supported by the National Science Foundation under Grant No. ACI-1548562.

■ REFERENCES

(1) Chheda, J. N.; Huber, G. W.; Dumesic, J. A. Liquid-phase catalytic processing of biomass-derived oxygenated hydrocarbons to fuels and chemicals. *Angew. Chem., Int. Ed.* **2007**, *46*, 7164−7183.

(2) Liao, Y. T.; Matsagar, B. M.; Wu, K. C. Metal-Organic Framework (MOF)-Derived Effective Solid Catalysts for Valorization of Lignocellulosic Biomass. *ACS Sustainable Chem. Eng.* **2018**, *6*, 13628−13643.

(3) Zhang, D.; Barri, S. A.; Chadwick, D. Dehydration of 1,2-propanediol to propionaldehyde over zeolite catalysts. *Appl. Catal., A* **2011**, *400*, 148−155.

(4) Mei, D.; Lercher, J. A. Effects of Local Water Concentrations on Cyclohexanol Dehydration in H-BEA Zeolites. *J. Phys. Chem. C* **2019**, *123*, 25255−25266.

(5) Mellmer, M. A.; Sener, C.; Gallo, J. M. R.; Luterbacher, J. S.; Alonso, D. M.; Dumesic, J. A. Solvent effects in acid-catalyzed biomass conversion reactions. *Angew. Chem., Int. Ed.* **2014**, *53*, 11872−11875.

(6) Mellmer, M. A.; Sanpitakseree, C.; Demir, B.; Bai, P.; Ma, K.; Neurock, M.; Dumesic, J. A. Solvent-enabled control of reactivity for liquid-phase reactions of biomass-derived compounds. *Nat. Catal.* **2018**, *1*, 199−207.

(7) Walker, T. W.; Chew, A. K.; Li, H.; Demir, B.; Zhang, Z. C.; Huber, G. W.; Van Lehn, R. C.; Dumesic, J. A. Universal kinetic solvent effects in acid-catalyzed reactions of biomass-derived oxygenates. *Energy Environ. Sci.* **2018**, *11*, 617−628.

(8) Varghese, J. J.; Mushrif, S. H. Origins of complex solvent effects on chemical reactivity and computational tools to investigate them: a review. *React. Chem. Eng.* **2019**, *4*, 165−206.

(9) Mellmer, M. A.; Sanpitakseree, C.; Demir, B.; Ma, K.; Elliott, W. A.; Bai, P.; Johnson, R. L.; Walker, T. W.; Shanks, B. H.; Rioux, R. M.; Neurock, M.; Dumesic, J. A. Effects of chloride ions in acid-catalyzed biomass dehydration reactions in polar aprotic solvents. *Nat. Commun.* **2019**, *10*, 1132.

(10) Mushrif, S. H.; Varghese, J. J.; Krishnamurthy, C. B. Solvation dynamics and energetics of intramolecular hydride transfer reactions in biomass conversion. *Phys. Chem. Chem. Phys.* **2015**, *17*, 4961.

(11) Piccini, G.; Lee, M.-S.; Yuk, S. F.; Zhang, D.; Collinge, G.; Kollias, L.; Nguyen, M.-T.; Glezakou, V.-A.; Rousseau, R. Ab initio molecular dynamics with enhanced sampling in heterogeneous catalysis. *Catal. Sci. Technol.* **2022**, *12*, 12−37.

(12) Velasco Calderón, J. C.; Jiang, S.; Mushrif, S. H. Understanding the Effect of Solvent Environment on the Interaction of Hydronium Ion with Biomass Derived Species: A Molecular Dynamics and Metadynamics Investigation. *ChemPhysChem* **2021**, *22*, 2222.

(13) Kowsari, M. H.; Tohidifar, L. Systematic evaluation and refinement of existing all-atom force fields for the simulation of liquid acetonitrile. *J. Comput. Chem.* **2018**, *39*, 1843−1853.

(14) Vishnyakov, A.; Lyubartsev, A. P.; Laaksonen, A. Molecular dynamics simulations of dimethyl sulfoxide and dimethyl sulfoxide-water mixture. *J. Phys. Chem. A* **2001**, *105*, 1702−1710.

(15) Colombari, F. M.; de Moura, A. F.; Freitas, L. C. G. Chiral recognition of liquid phase dimers from gamma-valerolactone racemic mixture. *J. Mol. Model.* **2018**, *24*, 215.

(16) Lin, H.; Truhlar, D. G. QM/MM: What have we learned, where are we, and where do we go from here? *Theor. Chem. Acc.* **2007**, *117*, 185−199.

(17) Lu, X.; Fang, D.; Ito, S.; Okamoto, Y.; Ovchinnikov, V.; Cui, Q. QM/MM free energy simulations: recent progress and challenges. *Mol. Simul.* **2016**, *42*, 1056−1078.

(18) Roßbach, S.; Ochsenfeld, C. Influence of Coupling and Embedding Schemes on QM Size Convergence in QM/MM Approaches for the Example of a Proton Transfer in DNA. *J. Chem. Theory Comput.* **2017**, *13*, 1102−1107.
(19) Caratzoulas, S.; Vlachos, D. G. Converting fructose to 5-hydroxymethylfurfural: A quantum mechanics/molecular mechanics study of the mechanism and energetics. *Carbohydr. Res.* **2011**, *346*, 664−672.
(20) Schwarz, K.; Sundararaman, R. The electrochemical interface in first-principles calculations. *Surf. Sci. Rep.* **2020**, *75*, 100492.
(21) Lim, H. K.; Lee, H.; Kim, H. A Seamless Grid-Based Interface for Mean-Field QM/MM Coupled with Efficient Solvation Free Energy Calculations. *J. Chem. Theory Comput.* **2016**, *12*, 5088−5099.
(22) Clabaut, P.; Schweitzer, B.; Götz, A. W.; Michel, C.; Steinmann, S. N. Solvation Free Energies and Adsorption Energies at the Metal/Water Interface from Hybrid Quantum-Mechanical/Molecular Mechanics Simulations. *J. Chem. Theory Comput.* **2020**, *16*, 6539−6549.
(23) Chew, A. K.; Jiang, S.; Zhang, W.; Zavala, V. M.; Van Lehn, R. C. Fast predictions of liquid-phase acid-catalyzed reaction rates using molecular dynamics simulations and convolutional neural networks. *Chem. Sci.* **2020**, *11*, 12464−12476.
(24) Maldonado, A. M.; Basdogan, Y.; Berryman, J. T.; Rempe, S. B.; Keith, J. A. First-principles modeling of chemistry in mixed solvents: Where to go from here? *J. Chem. Phys.* **2020**, *152*, 130902.
(25) Frisch, M. J., Trucks, G. W., Schlegel, H. B., Scuseria, G. E., Robb, M. A., Cheeseman, J. R., Scalmani, G., Barone, V., Petersson, G. A., Nakatsuji, H., Li, X., Caricato, M., Marenich, A., Bloino, J., Janesko, B. G., Gomperts, R., Mennucci, B., Hratchian, H. P., Ort, J. V.*Gaussian 09, Revision A.02*. 2016.
(26) Becke, A. D. Density-functional thermochemistry. III. The role of exact exchange. *J. Chem. Phys.* **1993**, *98*, 5648−5652.
(27) Schlegel, H. B. Optimization of Equilibrium Geometries and Transition Structures. *J. Comput. Chem.* **1982**, *3*, 214−218.
(28) Mennucci, B.; Cammi, R.; Tomasi, J. Excited states and solvatochromic shifts within a nonequilibrium solvation approach: A new formulation of the integral equation formalism method at the self-consistent field, configuration interaction, and multiconfiguration self-consistent field level. *J. Chem. Phys.* **1998**, *109*, 2798−2807.
(29) Kirkwood, J. G. Statistical Mechanics of Fluid Mixtures. *J. Chem. Phys.* **1935**, *3*, 300−313.
(30) Straatsma, T. P.; Berendsen, H. J. C. Free energy of ionic hydration: Analysis of a thermodynamic integration technique to evaluate free energy differences by molecular dynamics simulations. *J. Chem. Phys.* **1988**, *89*, 5876−5886.
(31) Straatsma, T. P.; Berendsen, H. J. C.; Postma, J. P. M. Free energy of hydrophobic hydration: A molecular dynamics study of noble gases in water. *J. Chem. Phys.* **1986**, *85*, 6720−6727.
(32) Hess, B.; van der Vegt, N. F. Hydration thermodynamic properties of amino acid analogues: A systematic comparison of biomolecular force fields and water models. *J. Phys. Chem. B* **2006**, *110*, 17616−17626.
(33) Shivakumar, D.; Williams, J.; Wu, Y.; Damm, W.; Shelley, J.; Sherman, W. Prediction of absolute solvation free energies using molecular dynamics free energy perturbation and the opls force field. *J. Chem. Theory Comput.* **2010**, *6*, 1509−1519.
(34) Berendsen, H.; van der Spoel, D.; van Drunen, R. GROMACS A message-passing parallel molecular dynamics implementation. *Comput. Phys. Commun.* **1995**, *91*, 43−56.
(35) Lindahl, E.; Hess, B.; van der Spoel, D. GROMACS 3.0: a package for molecular simulation and trajectory analysis. *J. Mol. Model.* **2001**, *7*, 306−317.
(36) Van Der Spoel, D.; Lindahl, E.; Hess, B.; Groenhof, G.; Mark, A. E.; Berendsen, H. J. C. GROMACS: Fast, flexible, and free. *J. Comput. Chem.* **2005**, *26*, 1701−1718.
(37) Hess, B.; Kutzner, C.; van der Spoel, D.; Lindahl, E. GROMACS 4: Algorithms for Highly Efficient, Load-Balanced, and Scalable Molecular Simulation. *J. Chem. Theory Comput.* **2008**, *4*, 435−447.
(38) Pronk, S.; Páll, S.; Schulz, R.; Larsson, P.; Bjelkmar, P.; Apostolov, R.; Shirts, M. R.; Smith, J. C.; Kasson, P. M.; van der Spoel, D.; Hess, B.; Lindahl, E. GROMACS 4.5: a high-throughput and highly parallel open source molecular simulation toolkit. *Bioinformatics* **2013**, *29*, 845−854.
(39) Abraham, M. J.; Murtola, T.; Schulz, R.; Páll, S.; Smith, J. C.; Hess, B.; Lindahl, E. GROMACS: High performance molecular simulations through multi-level parallelism from laptops to supercomputers. *SoftwareX* **2015**, *1-2*, 19−25.
(40) Jorgensen, W. L.; Maxwell, D. S.; Tirado-Rives, J. Development and Testing of the OPLS All-Atom Force Field on Conformational Energetics and Properties of Organic Liquids. *J. Am. Chem. Soc.* **1996**, *118*, 11225−11236.
(41) Jorgensen, W. L.; Chandrasekhar, J.; Madura, J. D.; Impey, R. W.; Klein, M. L. Comparison of simple potential functions for simulating liquid water. *J. Chem. Phys.* **1983**, *79*, 926−935.
(42) Martínez, L.; Andrade, R.; Birgin, E. G.; Martínez, J. M. PACKMOL: A package for building initial configurations for molecular dynamics simulations. *J. Comput. Chem.* **2009**, *30*, 2157−2164.
(43) Miyamoto, S.; Kollman, P. A. Settle: An analytical version of the SHAKE and RATTLE algorithm for rigid water models. *J. Comput. Chem.* **1992**, *13*, 952−962.
(44) Bussi, G.; Donadio, D.; Parrinello, M. Canonical sampling through velocity rescaling. *J. Chem. Phys.* **2007**, *126*, 014101.
(45) Berendsen, H. J.; Postma, J. P.; van Gunsteren, W. F.; DiNola, A.; Haak, J. R. Molecular dynamics with coupling to an external bath. *J. Chem. Phys.* **1984**, *81*, 3684−3690.
(46) Singh, U. C.; Kollman, P. A. An approach to computing electrostatic charges for molecules. *J. Comput. Chem.* **1984**, *5*, 129−145.
(47) Besler, B. H.; Merz, K. M.; Kollman, P. A. Atomic charges derived from semiempirical methods. *J. Comput. Chem.* **1990**, *11*, 431−439.
(48) Kirchner, B. Eigen or zundel ion: News from calculated and experimental photoelectron spectroscopy. *ChemPhysChem* **2007**, *8*, 41−43.
(49) Dahms, F.; Costard, R.; Pines, E.; Fingerhut, B. P.; Nibbering, E. T.; Elsaesser, T. The Hydrated Excess Proton in the Zundel Cation H5O2+: The Role of Ultrafast Solvent Fluctuations. *Angew. Chem., Int. Ed.* **2016**, *55*, 10600−10605.
(50) Dahms, F.; Fingerhut, B. P.; Nibbering, E. T. J.; Pines, E.; Elsaesser, T. Large-amplitude transfer motion of hydrated excess protons mapped by ultrafast 2D IR spectroscopy. *Science* **2017**, *357*, 491−495.
(51) Daly, C. A.; Streacker, L. M.; Sun, Y.; Pattenaude, S. R.; Hassanali, A. A.; Petersen, P. B.; Corcelli, S. A.; Ben-Amotz, D. Decomposition of the Experimental Raman and Infrared Spectra of Acidic Water into Proton, Special Pair, and Counterion Contributions. *J. Phys. Chem. Lett.* **2017**, *8*, 5246−5252.
(52) Fournier, J. A.; Carpenter, W. B.; Lewis, N. H.; Tokmakoff, A. Broadband 2D IR spectroscopy reveals dominant asymmetric H5O2+ proton hydration structures in acid solutions. *Nat. Chem.* **2018**, *10*, 932−937.
(53) Calio, P. B.; Li, C.; Voth, G. A. Resolving the Structural Debate for the Hydrated Excess Proton in Water. *J. Am. Chem. Soc.* **2021**, *143*, 18672−18683.
(54) Klein, D. R.*Organic Chemistry*, 3rd ed.; Wiley, 2017; p 1312.
(55) Sofronov, O. O.; Bakker, H. J. Energy Relaxation and Structural Dynamics of Protons in Water/DMSO Mixtures. *J. Phys. Chem. B* **2018**, *122*, 10005−10013.
(56) Chew, A. K.; Van Lehn, R. C. Quantifying the stability of the hydronium ion in organic solvents with molecular dynamics simulations. *Front. Chem.* **2019**, *7*, 439.
(57) Tran, B.; Cai, Y.; Janik, M. J.; Milner, S. T. Hydrogen bond thermodynamics in aqueous acid solutions: a combined DFT and classical force-field approach. *J. Phys. Chem. A* **2022**, *136*, 7382−7398, DOI: 10.1021/acs.jpca.2c04124.

(58) Mushrif, S. H.; Caratzoulas, S.; Vlachos, D. G. Understanding solvent effects in the selective conversion of fructose to 5-hydroxymethyl-furfural: A molecular dynamics investigation. *Phys. Chem. Chem. Phys.* **2012**, *14*, 2637−2644.
(59) Kim, Y.; Mittal, A.; Robichaud, D. J.; Pilath, H. M.; Etz, B. D.; St. John, P. C.; Johnson, D. K.; Kim, S. Prediction of hydroxymethylfurfural yield in glucose conversion through investigation of lewis acid and organic solvent effects. *ACS Catal.* **2020**, *10*, 14707−14721.

https://doi.org/10.1021/acscatal.2c03978
ACS Catal. 2022, 12, 13193−13206